www.springer.com/41230
https://doi.org/10.1007/s41230-022-1183-2
Research & Development
Vol. 19 No. 2 March 2022
CHINA FOUNDRY

Effects of cooling rates on microporosity in DC casting Al-Li alloy

Yu-xuan Zhang[1], *Jun-sheng Wang[1, 2], Dong-xu Chen[1], Bing Wang[1], Chi Zhang[1], and Zheng-an Wang[3]

1. School of Materials Science and Engineering, Beijing Institute of Technology, Beijing 100081, China

2. Advanced Research Institute of Multidisciplinary Science, Beijing Institute of Technology, Beijing 100081, China

3. Chinalco Southwest Aluminium (Group) Co., Ltd., Chongqing 401326, China

Abstract: During the direct chill (DC) casting process, primary cooling from the mold and bottom block, and secondary cooling from the waterjets produce a concave solid shell. The depth of this liquid pocket and mushy zone not only depends on the solidification range of the alloy but also the boundary conditions such as cooling rates. Al-Li alloys solidify in a long solidification range increasing the susceptibility of porosity nucleation in the semi-solid region. In this study, the effects of cooling rate on the porosity formation were quantified for the large ingot casting using X-ray computed tomography (XCT). By characterizing pore size distributions at four different cooling conditions, the correlation between the mechanical properties at both room and high temperatures and the microstructure features was identified. The constitutive equations were constructed. It is found that increasing the cooling rate reduces the grain size, increases the number density of micropores, and minimizes the number of large pores, thereby improving the mechanical performance. Therefore, long mushy zones and deep liquid pockets in Al-Li alloys can be effectively controlled by controlling the boundary conditions of the DC casting solidification process, thereby obtaining castings with excellent mechanical properties.

Keywords: Al-Li alloys; microporosity; cooling rate; XCT; constitutive equation

CLC numbers: TG146.21 **Document code:** A **Article ID:** 1672-6421(2022)02-177-14

1 Introduction

As a key lightweight and high-strength structural material, aluminum-lithium alloys have the characteristics of high specific strength and rigidity, and are cheaper than carbon fiber composite materials, so these alloys are widely used in the aerospace industry [1-3]. AA2297 aluminum alloy is one of the third-generation aluminum-lithium alloys and has many excellent properties including high modulus and specific strength. Therefore, it has been widely used for constructing the rocket launch system and modern fuel economy aircrafts [4-6]. At present, direct chill (DC) casting is the major production route for large aluminum-lithium alloy ingots or billets [7, 8]. In this process, controlling the formation of internal defects in the alloy is the key to achieve high-performance ingots. To date, many studies have been focusing on the mechanisms of defect formation, such as segregation and porosity. The long solidification range of Al-Li alloys results in a large number of internal micropores, and these defects often degrade the performance of the final product [9-11]. With the increasing demand for light weight airframe structures, high quality casting ingots with few defects have become the key objective of achieving high strength Al-Li alloys [12, 13].

The hydrogen supersaturation is the major cause of porosity in Al-Li alloys due to the elevated hydrogen solubility in the Li-containing liquid. During solidification, the solubility of hydrogen in liquid Al-Li alloys is 10 times than that of the alloy without Li, and its solubility in the solid is reduced to such a level that it will only dissolve one twentieth of that amount as in the liquid [14], transforming the excess amount of hydrogen into gas bubbles. In addition, due to the long solidification range for Al-Li alloys, the segregation of hydrogen is exaggerated when there is enough time for the hydrogen diffusion into such areas as oxide impurities, grain boundaries, and ceramic particles. Therefore, the accumulation of hydrogen is not only a function of the diffusion of hydrogen

***Jun-sheng Wang**

Professor in the Advanced Research Institute of Multidisciplinary Sciences, Beijing Institute of Technology and Ph.D from Imperial College London, UK and specialized in ultra-light alloy design and manufacture process optimization using Integrated Computational Materials Engineering (ICME), and leading several national key projects to realize integrated design and intelligent manufacturing.

E-mail: junsheng.wang@bit.edu.cn

Received: 2021-10-12; Accepted: 2022-02-25

in the mushy zone, but also a function of cooling rate [15-17]. Anyalebechi et al. [18] initially studied the temperature-dependent behavior of hydrogen solubility in Al-Li binary solid alloys. On this basis, Anyalebechi [19, 20] and others then used Wagner interaction parameters to analyze the effects of different alloying elements and temperature on the solubility and thermodynamic behavior of hydrogen in molten aluminum, and predicted the solubility of hydrogen at 973–1,123 K. In agreement with the experimental results, the solubility of hydrogen was found to increase with increasing temperature. Smith et al. [21] studied the effects of hydrogen on the porosity defects in Al-Li-Cu-Zr alloys, and found that the hydrogen content at the grain boundaries was higher than the interiors of grains. It was believed that hydrogen had an important influence on the generation of cracks and pores at the grain boundaries. Therefore, it is critical to understand the difference in hydrogen solubility at different cooling rates and to quantify the evolution of porosity morphology and size, which facilitates subsequent explorations of processing conditions to suppress porosity formation and improve the mechanical properties of Al-Li alloys [22].

To observe the internal porosity in Al-Li alloys, with the development of X-ray computed tomography (XCT) technology, Lee et al. [23] quantified the kinetics of microporosity formation in directional solidification and simulated the formation of pores in the alloy solidification process. Combined with the results of XCT experiments, the physical process of pore formation was deeply studied. Lee and Chaijaruwanich [24, 25] used XCT technology to study the evolution of pores during homogenization heat treatment after direct cooling (DC) cast Al-Mg alloy. Wang et al. [26] simulated pores in Al-Cu, Al-Si and Al-Si-Cu alloys and compared them with XCT three-dimensional reconstruction. The influence of different alloying additions on the internal microporosity was studied, and the concepts of sphericity and distortion factor were proposed to describe the three-dimensional morphology of micropores. Based on the method of studying aluminum alloy pores using XCT technology, took Al-Si-Cu alloys as an example, Wang et al. [27] conducted in-situ observations on the formation kinetics of iron-rich intermetallic compounds in aluminum alloys. Using XCT technology, the changes of the three-dimensional morphology and size distribution of Fe-rich intermetallic compounds at different Fe levels were studied. The influences of intermetallic compounds on the pore size distribution in Al castings were predicted [28]. However, most of the current research works are purely based on XCT scanning and 3D reconstruction to generate statistical data on the internal micropores of the alloy, and few studies have quantified the micropores in Al-Li alloy ingots as a function of the cooling rate during the DC casting process.

In this study, the microporosity defects in AA2297 Al-Li DC casting ingots were quantitatively studied. The finite element (FE) model was constructed using high temperature tensile testing results at various temperatures. The XCT quantification was subsequently performed on the specimens with different cooling rates, and the number, morphology and size of the pores were statistically quantified. The effects of cooling rate on the porosity in AA2297 Al-Li alloys were investigated, which can be used to optimize the mechanical properties of DC casting alloys.

2 Materials and experimental procedure

2.1 Materials

The materials in this study were from a commercial AA2297 Al-Li alloy ingot manufactured by the Southwest Aluminum Co. The DC casing AA2297 Al-Li alloy process diagram and its ingot bulk are shown in Figs. 1(a, b). The chemical composition of AA2297 Al-Li alloy measured using inductively coupled plasma-optical emission spectrometry (ICP-OES) is shown in Table 1.

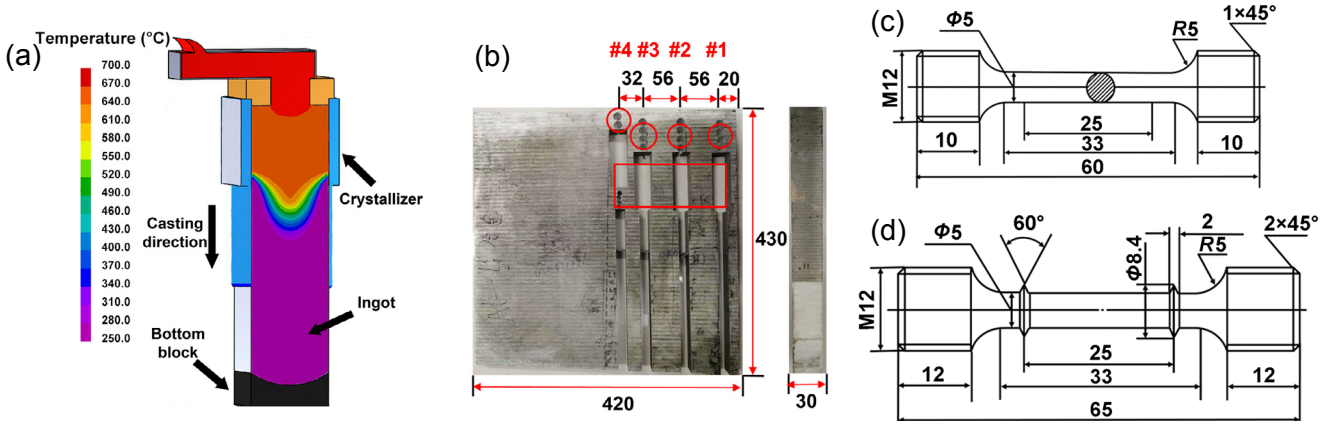

Fig. 1: Sampling from DC casting of AA2297: (a) production process with colors showing the cross-section temperature distribution; (b) a slice of 430 mm×420 mm×30 mm from the entire ingot with sampling locations; (c) coupon size for high temperature tests; (d) room temperature test specimen geometry (unit: mm)

Table 1: Chemical compositions of AA2297 casting ingot

Element	Cu	Li	Si	Mn	Mg	Ti	Fe	Zr	Al
Content (wt.%)	2.820	1.390	0.018	0.300	0.030	0.020	0.050	0.100	Bal.

The ingot bulk used in this experiment was obtained by cutting the large ingot into the size specification of 430 mm×420 mm×30 mm, and the geometric shape is shown in Fig. 1(b). Samples at different cooling rates were taken from the surface to the center of the ingot, and were numbered #1, #2, #3, and #4, respectively. The circles marked in Fig. 1(b) are the sample locations for the X-ray computed tomography (XCT) experiments, and the rectangle is the sample position for tensile tests and optical microscopy (OM) imaging.

2.2 Thermophysical properties and finite element model

The thermophysical properties of the AA2297 aluminum alloy were calculated by thermodynamic software Pandat, and the results are shown in Table 2.

The thermodynamic properties of AA2297 Al-Li alloy were written into the user database of the commercial finite element analysis software ProCast. The pouring temperature of this model was set slightly higher than the liquidus temperature, which was 677 °C. The flow rate for stable filling of molten metal was 0.23 kg·s^{-1}. The cooling water flow was controlled by the boundary conditions at Γ_4, and the empirical boiling water curve was used. Combining with relevant literature and engineering practice, the casting speed of this model was a constant at 1.7 mm·s^{-1}.

Figure 2 shows a schematic diagram of the model and the boundary conditions. The two-dimensional axisymmetric

Table 2: Thermophysical properties of AA2297 aluminum alloy

Temperature (°C)	Thermal conductivity [W·(m·K)$^{-1}$]	Expansion coefficient (×10^{-6} K^{-1})	Latent heat (kJ·kg^{-1})	Specific heat [J·(kg·K)$^{-1}$]	Density (kg·m^{-3})	Young's modulus (GPa)	Poisson's ratio
20	119.16	23.90	0.00	0.92	2615.64	76.40	0.336
100	126.31	24.73	0.00	0.97	2601.12	73.91	0.339
200	132.00	25.85	0.00	1.02	2580.65	70.21	0.343
300	135.35	26.99	0.00	1.06	2558.72	66.08	0.348
400	137.40	28.17	0.00	1.10	2535.34	61.52	0.354
500	138.52	29.33	0.00	1.19	2510.77	56.53	0.361
510	138.60	29.51	413.47	1.89	2508.24	56.01	0.361
530	139.60	31.67	393.92	3.18	2495.68	46.78	0.370
570	133.52	35.39	366.22	1.59	2473.10	33.36	0.384
600	131.03	37.22	349.18	2.20	2458.64	26.41	0.392
630	122.18	40.96	293.83	6.85	2428.62	12.27	0.412
651	92.08	65.80	51.85	33.28	2328.87	0.01	0.460
660	87.56	70.46	0.35	1.20	2306.53	0.00	0.480

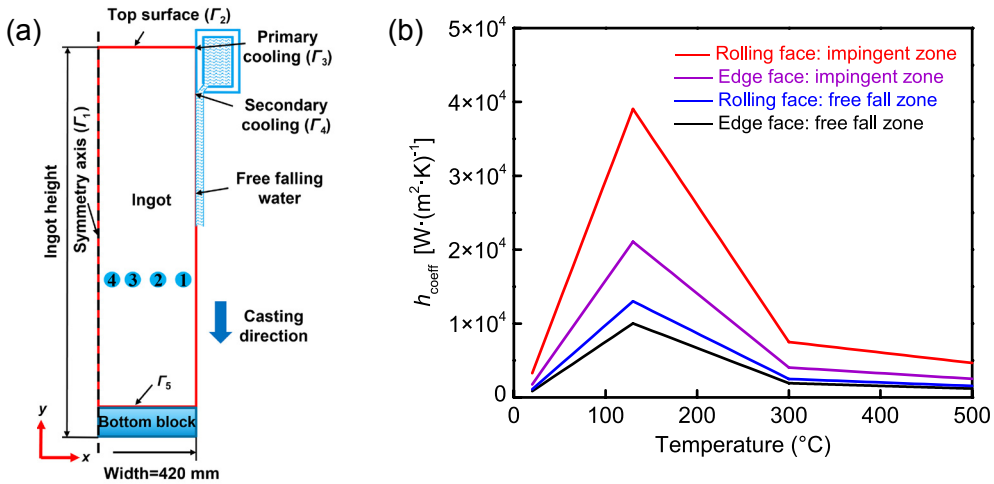

Fig. 2: DC casting model: (a) schematic of boundary condition (B.C.), and heat transfer coefficient (HTC) for secondary water cooling (impingement water cooling) of AA2297 casting ingot (b)

coupling thermomechanical model in ProCast was used to simulate the DC casting process of the AA2297 ingot. The boundary conditions of the model are: v_x=0 and v_z=0 at the intersection of the centerline and the bottom of the ingot to restrict the movement of the ingot in the x and z directions. Different thermal boundary conditions are set in different cooling methods. The symmetry axis (Γ_1) and the top surface (Γ_2) are set as adiabatic boundaries. On the primary cooling surface (Γ_3), the heat transfer coefficient changes with the solid fraction of the liquid metal. According to the previous work and related references [29-31], the total heat transfer coefficient at Γ_3 [W·(m^2·K)$^{-1}$] is expressed as:

$$h_{\Gamma_3} = h_{\text{contact}}(1-f_s) + h_{\text{gap}} \cdot f_s \quad (1)$$

where h_{Γ_3} is the total heat transfer coefficient, h_{contact} is the heat transfer coefficient when the contact is good, f_s is the fraction of contact, h_{gap} is the heat transfer coefficient of the air gap between the ingot and the mold. The secondary cooling surface (Γ_4) is divided into the impingent zone and the free falling zone. In these two areas, the main method of heat transfer is boiling water heat transfer. According to the Refs. [32, 33] and engineering practice, the empirical boiling water curve of this model satisfies Eq. (2):

$$h_{\Gamma_4} = k_{\text{rolling/edge}}(s \cdot T + i) \quad (2)$$

where h_{Γ_4} is the heat transfer coefficient of the secondary cooling surface, $k_{\text{rolling/edge}}$ is the proportional coefficient in the length or width direction of the surface of the ingot, T is the surface temperature of the ingot (K), s and i are the coefficients related to the cooling water flow. The empirical boiling water curve used in the Γ_4 zone is shown in Fig. 2(b), and the heat transfer coefficient (Γ_5) at the bottom is set to 1,000 W·(m^2·K)$^{-1}$.

2.3 Microstructure characterization and XCT analysis

According to the standard process of metallographic sample preparation, the metallographic observation samples were ground with 400, 600, 800, 1,000, 1,500 and 2,000 grit SiC sandpapers firstly, and then polished with 3.5 μm and 1 μm diamond polishing agents. Their metallographs were then observed by an optical microscope (OM, LWD200-4XC). Afterwards, Keller's reagent solution (95% H_2O, 2.5% HNO_3, 1.5% HCl and 1.0% HF) was used to corrode the samples with different cooling rates to measure the grain size. A cold field emission scanning electron microscope (FE-SEM, HITACHI UHR SU8200 Series) was used to characterize the structure, intermetallic compound composition and tensile fracture surface morphology.

X-ray computed tomography experiments were performed using a Zeiss Xradia 520 Versa device to quantify the hydrogen pores at different cooling rates. In XCT experiments, the target power was set at 7 W and the acceleration voltage was chosen as 80 kV. The cross-section of each sample was characterized by a 2,000×2,000 high-resolution camera. A total of 2,001 images were collected at 360°, and then they were reconstructed into 3D voxels with a voxel size of 0.65 μm×0.65 μm×0.65 μm. Three-dimensional visualization was performed using DragonFly software, and the size (equivalent diameter), morphology (sphericity) and number density distribution of porosity with an equivalent diameter greater than 5 μm were calculated and analyzed. The equivalent diameter (d) is the spherical diameter occupying the same volume as the quantified geometry; the sphericity (S_p) is defined as the ratio of the surface area (A) of the equal volume sphere to the actual surface area of the micropores. The formulas of d and S_p are given as [34, 35]:

$$d = \sqrt[3]{6V/\pi} \quad (3)$$

$$S_p = \sqrt[3]{36\pi V^2/A} \quad (4)$$

where V and A are the actual volume and surface area of each micropore, respectively.

2.4 Mechanical performance

The digital micro hardness tester (TMVS-1) was used for hardness analysis. The load was set to 200 g for 10 s, and 13 measurements were performed on each sample. Tensile samples were then taken according to Fig. 1(b), numbered #1, #2, #3, and #4, respectively. The sampling dimensions of room and high temperatures are shown in Figs. 1(c) and 1(d). The room temperature and high temperature tensile tests were carried out using Suns UTM6104 electronic universal testing machine and MTS-E45 testing machine with a 25 mm fixed extensometer, respectively. Tensile tests were performed on samples with different cooling rates at room temperature with a strain rate of 1 mm·min^{-1}. Tensile experiments for deriving the constitutive equation of AA2297 Al-Li alloy were performed at 5 different temperatures (25 °C, 100 °C, 200 °C, 300 °C, and 400 °C) and 3 different strain rates (10^{-2} mm·s^{-1}, 10^{-3} mm·s^{-1}, and 10^{-4} mm·s^{-1}). Among them, the high temperature tensile samples need to be heated to the set temperature and held for 45 min. Subsequently, the SEM/EDS was used to characterize the fracture surface and analyze crack initiators.

2.5 Constitutive equation

The constitutive equation below the solidus temperature is based on the extended Ludwik equation [36], as shown in the following equation:

$$\sigma = K(\varepsilon_p + \varepsilon_{p_0})^n(\dot{\varepsilon}_p + \dot{\varepsilon}_{p_0})^m \quad (5)$$

where σ is the stress (MPa), K is the materials constant related to the strength (MPa), ε_p is the total plastic strain, $\dot{\varepsilon}_p$ is the equivalent plastic strain rate (s^{-1}), m is the strain rate sensitivity coefficient, and n is the strain hardening factor. K, m and n are all temperature-related parameters, and their values are fitted according to the tensile test data at different temperatures and strain rates. To simplify the model and achieve rapid convergence of the equation, the two coefficients ε_{p_0} and $\dot{\varepsilon}_{p_0}$ are set to 1×10^{-6} and 1×10^{-4}, respectively, according to the relevant literature [36].

3 Results

3.1 FEM simulation of cooling rates as a function of locations

Finite element analysis software (ProCast) was used to simulate the temperature field and solid fraction of the sample during the solidification and cooling of the DC cast AA2297 Al-Li alloy, and the results are shown in Figs. 2(a) and (b). It can be found that the temperature field distribution at different positions of the ingot is very different from the surface to the center. The sampling position was set at about 110 cm from the bottom of the ingot. As shown in Figs. 3(c)–(f), the curves of temperature change with time from the Position #1 of the ingot surface to the Position #4 of the center of the ingot are extracted respectively. On the basis of the temperature curves, the first-order derivations were calculated, and the curves of the cooling rate change with time were obtained. It can be found from the first-order derivations that there is a big difference in the cooling rates between the surface and the center of the ingot. The fastest cooling rate of the sample at the surface Position #1 can reach 3.49 °C·s^{-1}. The cooling rates of the #2 and #3 positions are 1.53 °C·s^{-1} and 0.96 °C·s^{-1}, respectively, while the cooling rate of the center Position #4 is only 0.83 °C·s^{-1}.

3.2 Microstructure characteristics at different cooling rates

The microstructure of the DC casting AA2297 Al-Li is mainly composed of dendrites, as shown in Fig. 4. There are significant differences in the morphology and size of the crystal grains at different cooling rates. With the increase of cooling rate from 0.83 °C·s^{-1} to 3.94 °C·s^{-1}, the grain refinement occurs, the number of crystal grains increases significantly, and the grain size decreases. The grain sizes of #1, #2, #3 and #4 are

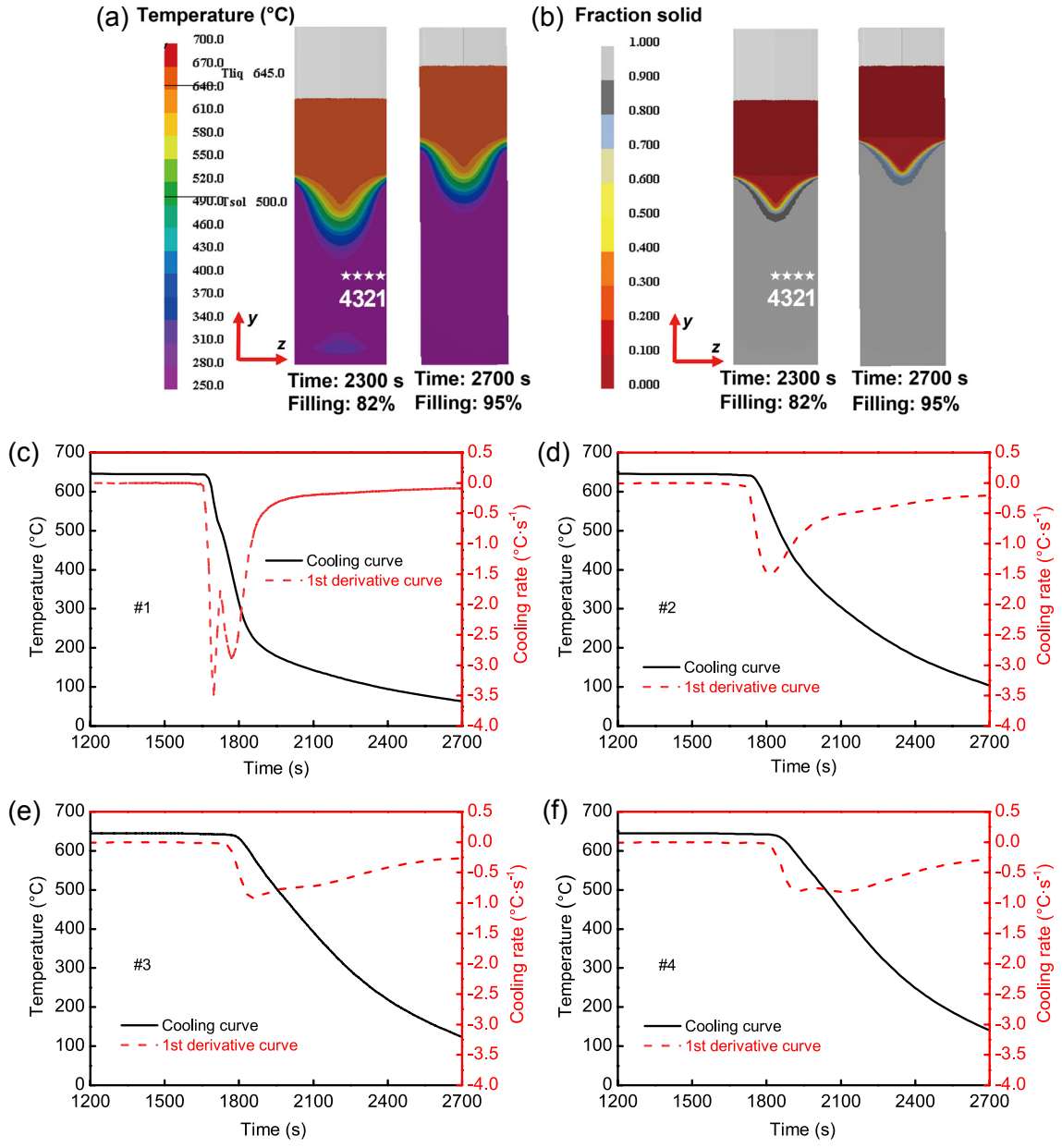

Fig. 3: Temperature/cooling rates as a function of time: contour plot of temperature (a) and solid fraction (b) at 82% and 95% filling; temperature and cooling rates for Positions #1 (c), #2 (d), #3 (e), and #4 (f)

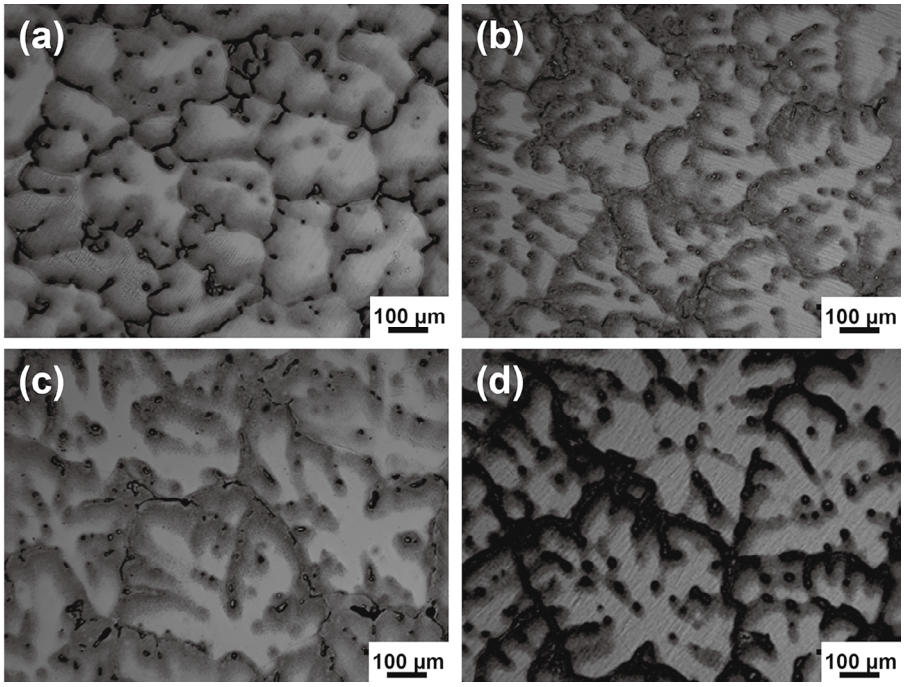

Fig. 4: Optical metallograph of Al-Li casting samples at different cooling rates: (a) #1 at 3.49 °C·s^{-1}; (b) #2 at 1.53 °C·s^{-1}; (c) #3 at 0.96 °C·s^{-1}; (d) #4 at 0.83 °C·s^{-1}

about 200 μm, 300 μm, 400 μm, and 450 μm, respectively. The reason is that the position of Sample #4 is close to the center, the cooling rate is low, and the nucleus has sufficient time to grow, resulting in coarse grains and secondary dendritic arms; while the position of Sample #1 is in the outermost side of the ingot, where the cooling rate is faster than at #4, the nucleus has not enough time to grow, and so the grain is small.

Figure 5 shows SEM images of the DC casting AA2297 Al-Li alloy at different cooling rates. It is found cooling rate has no significant effect on the number of intermetallic compounds, the vast majority of which are gray particles distributed mainly in long, spherical shapes along the grain boundaries in the aluminum alloy matrix. EDS results are shown in Table 3. It is found that the gray particles are mainly intermetallic compounds containing Al and Cu, while Li cannot be detected by EDS because the atomic mass of Li is too light. Using Pandat software to perform thermodynamic calculations, the relationship between solid phase fraction and temperature and the solidification path of precipitates under non-equilibrium solidification of 2297Al-Li alloy was obtained, as shown in Figs. 5(g, h). Combined with previous EDS tests and related Refs. [37, 38], it can be known that the main components of intermetallic compounds of gray particles include Al_2CuLi and Al_7Cu_4Li. Some dark gray slab-like particles in Fig. 5(f) are deposited on the gray particles, which are initially identified as intermetallic compounds containing Fe and Mn elements by EDS energy spectroscopy. In addition, it is observed that pores inside the alloy always form at the interdendritic region around the intermetallic compounds, because when the molten metal flow is blocked by the formed intermetallics, the bubbles are also limited by the growing dendrites during solidification. Tiny hydrogen pores are formed by the hydrogen atoms diffusion into the shrinkage cavity. They absorb the excess amount of hydrogen rejected by the growing dendrites and intermetallic particles, and eventually take up all the remaining space where both α-Al and eutectic Al_2Cu shrink, producing complex morphology. Besides, the presence of white intermetallic compounds around some of the pores [Fig. 5(e), Point 1] was detected by EDS and found to be mainly composed of oxygen-containing intermetallic compounds. It is speculated that their formation is due to the fact that, in addition to hydrogen, oxides and other inclusions also play a role as nucleation sites for pores.

3.3 Quantitative characterization of micropores

Figures 6(a–d) show the micrograph of internal pores with cooling rates of 3.49 °C·s^{-1}, 1.53 °C·s^{-1}, 0.96 °C·s^{-1}, and 0.83 °C·s^{-1}, respectively. By qualitative analysis, it is found that the porosity decreases with the increase of cooling rate. Further selecting typical pores to observe their morphology, it is found that most of the pores are approximately circular and elliptical in Samples #1 and #2, while the pores of Samples #3 and #4 show irregular elongated shapes. As the cooling rate increases, the morphology of the pores gradually changes from irregular shapes to regular round pores.

Photographs taken by XCT technique and then visualized using DragonFly software demonstrate the characteristics and distribution of pores in the DC casting AA2297 Al-Li alloy. The pores were extracted and labeled in red, as shown in Fig. 7. It can be seen that the difference in cooling rate has a significant effect on the distribution of pores in the sample. Figure 7(a) shows the Sample #1 located at the surface of the ingot with a cooling rate of 3.49 °C·s^{-1}, has a large quantity of small micro-porosity. When the cooling rate is reduced to 1.53 °C·s^{-1}, 0.96 °C·s^{-1}, and 0.83 °C·s^{-1}, as shown in Figs. 7(b–d), larger and more irregular pores start forming.

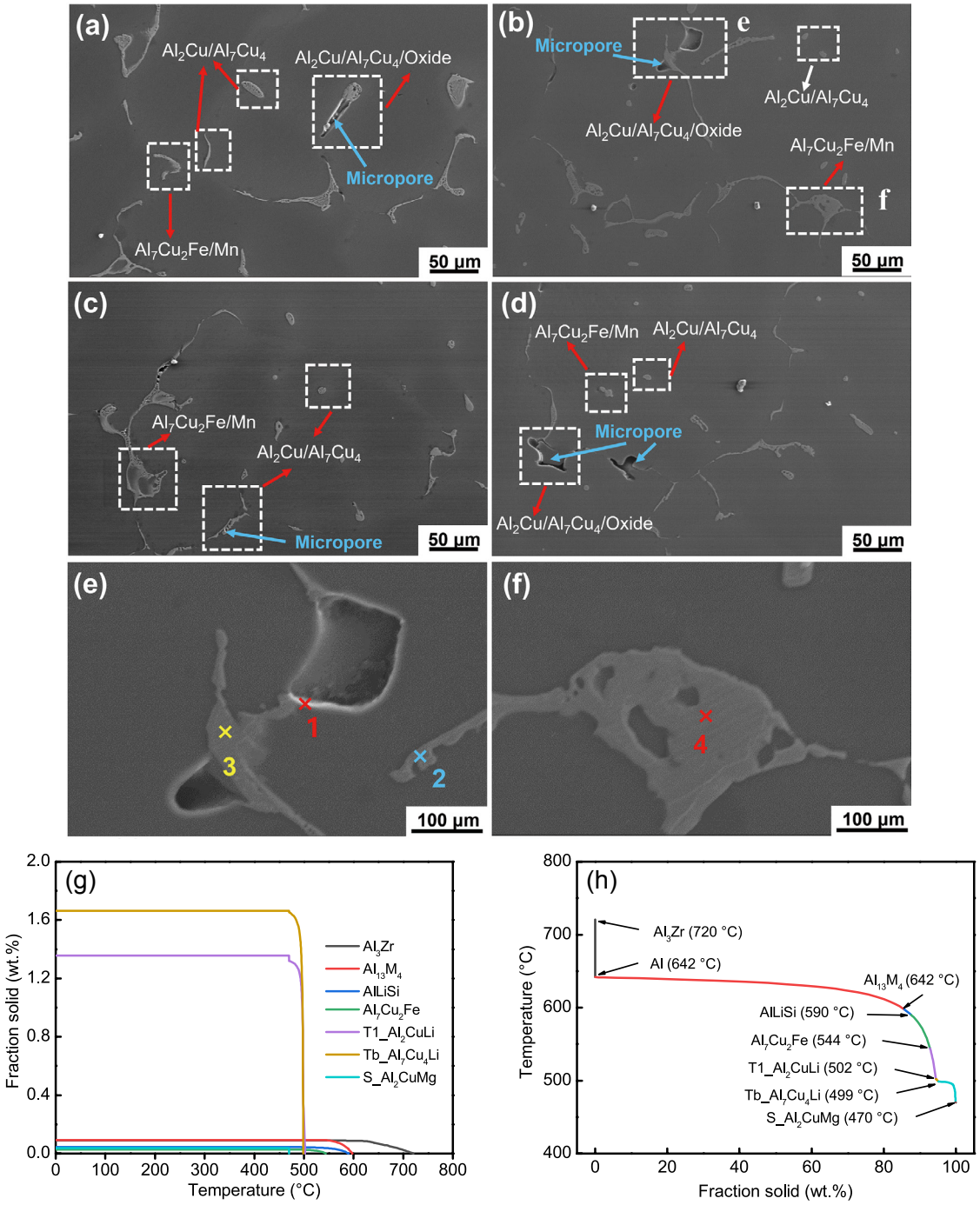

Fig. 5: SEM images of Al-Li casting ingots at different cooling rates and non-equilibrium solidification path calculation results: (a) #1 at 3.49 °C·s^{-1}; (b) #2 at 1.53 °C·s^{-1}; (c) #3 at 0.96 °C·s^{-1}; (d) #4 at 0.83 °C·s^{-1}; (e) and (f) enlarged images of EDS tests in selected areas in (b); (g) and (h) solid phase fraction and temperature relation graph, and solidification path diagram of precipitate under non-equilibrium solidification, respectively

Table 3: Composition of the intermetallic compounds measured by EDS in Figs. 5(e, f)

Point No.	Element (at.%)						Intermetallic compound
	Al	Cu	Mn	Fe	Si	O	
1	65.78	18.13	-	-	-	13.91	Oxide
2	70.93	29.07	-	-	-	-	Al_2Cu
3	65.21	34.79	-	-	-	-	Al_7Cu_4
4	69.10	18.98	3.37	8.55	-	-	Al_7Cu_2Mn/Fe

The number density and equivalent diameter distribution of the micropores are quantified in Fig. 8. The effects of cooling rates on the number density and equivalent diameter of micropores of AA2297 Al-Li alloy are significant. The equivalent diameters of the internal pores of the DC casting AA2297 Al-Li alloy are generally concentrated in the range of 5–9 μm, accounting for about 90% of the total pores. The maximum equivalent diameter of micropores decreases from 76.48 μm to 30.50 μm as the cooling rate increases from 0.83 °C·s^{-1} to 3.49 °C·s^{-1}, but the number of micropores increases significantly, especially the fine micropores. When the cooling rate of the samples is increased from 0.83 °C·s^{-1} for Sample #4 to 3.49 °C·s^{-1} for Sample #1, the density of micropores smaller than 7 μm change from 150 to 230 mm^{-3}. It is worth noting that the number density of pores and the maximum micropore equivalent diameter of Sample #2 fluctuate in data, which is different from the overall law. The reason for this phenomenon may be that the DC ingot is large, the positions of each sample are relatively close and the impurity segregation in #2 location may promote the hydrogen porosity formation, and also due to the accidental error caused by sampling in a small interval. There are differences in the cooling rate during the solidification process, and the growth time of the micropores is different, which causes the size of the micropores to be affected. Combined with the relevant references [39, 40], statistics in the range below 5 μm may contain a lot of noise. Therefore, in this study, the pores above 5 μm were selected for statistics, and the analysis in this range makes the results more effective and accurate.

The morphology of the pores also has a great influence on the fatigue life and mechanical properties. The differences between the typical pore morphology of Sample #1 (at the surface of the ingot) and Sample #4 (at the center of the ingot) are compared in Figs. 7(e) and (h). Table 4 shows the statistical values of the porosity (P), number density of pores (N), minimum sphericity (ε_{min}), maximum pore equivalent diameter (d_{max}), and

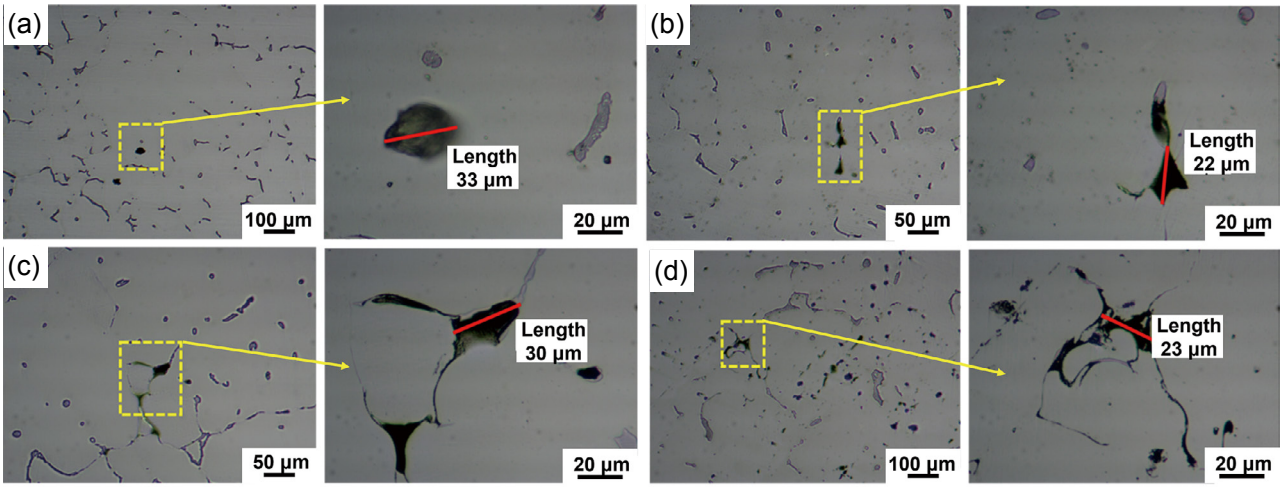

Fig. 6: Morphology and typical pores in as-cast AA2297 Al-Li alloy: (a) #1; (b) #2; (c) #3; (d) #4

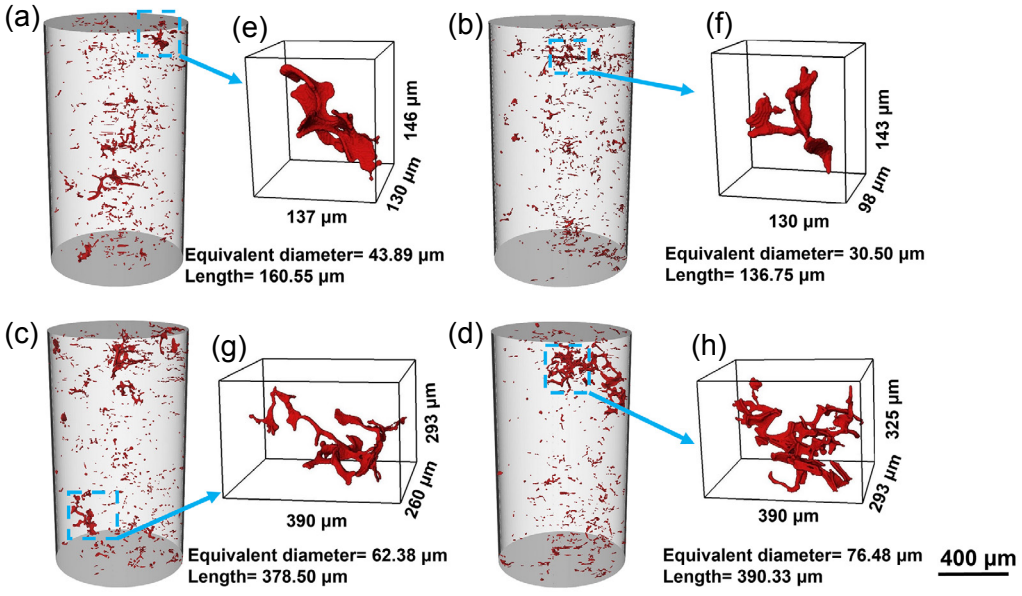

Fig. 7: 3D morphologies of micropores from XCT at four cooling rates: (a) 3.49 °C·s^{-1}; (b) 1.53 °C·s^{-1}; (c) 0.96 °C·s^{-1}; (d) 0.83 °C·s^{-1}; (e), (f), (g), (h) are the 3D structure diagrams of micropores with the largest equivalent diameters in (a), (b), (c), (d), respectively

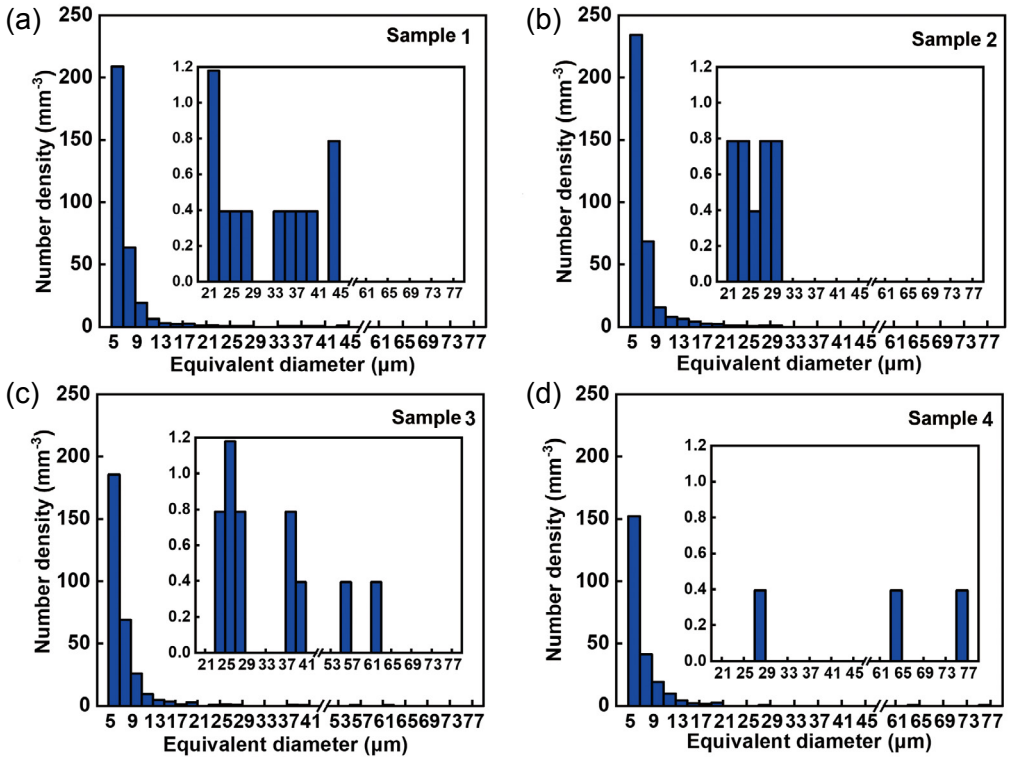

Fig. 8: Number density of micropores as a function of pore diameter at four cooling rates: (a) 3.49 °C·s^{-1}; (b) 1.53 °C·s^{-1}; (c) 0.96 °C·s^{-1}; (d) 0.83 °C·s^{-1}

Table 4: Porosity, number density, minimum sphericity, maximum equivalent micropore diameter and length of four samples

Sample	P (%)	N (mm^{-3})	d_{max} (μm)	L_{max} (μm)	ε_{min}
#1	0.081	310.66	43.89	231.19	0.23
#2	0.066	344.48	30.50	143.98	0.25
#3	0.104	306.12	62.38	378.50	0.16
#4	0.115	233.98	76.48	390.33	0.12

length (L_{max}), at different cooling rates. As it is well known in DC casting, there are macrosegregation of impurities towards the 2/3 location due to the thermo-solutal buoyancy. Impurity particles inevitably promote the nucleation of porosity which produces smaller pore for Sample #2 with large number density. As the cooling rate decreases, it is found that the maximum microporous equivalent diameter increases from 30.50 μm to 76.48 μm, the equivalent length increases from 143.98 μm to 390.33 μm, and the minimum sphericity decreases from 0.23 to 0.12. The shape of the large pores gradually becomes irregular, which is due to the reduced cooling rate leading to longer solidification time. The small pores will have sufficient time to gather and diffuse, and eventually form large irregular shaped pores. These large irregular pores will greatly affect the mechanical properties of the alloy.

3.4 Mechanical properties

3.4.1 Mechanical properties at room temperature

Figure 9 shows the microhardness values of the samples at different cooling rates. The average microhardness of Samples #1, #2, #3, and #4 are 70.2 HV, 67.3 HV, 63.5 HV, and 65.5 HV, respectively. The increase of cooling rate from 0.83 °C·s^{-1} to 3.49 °C·s^{-1} can raise the hardness value by about 8%. This indicates that refinement of grains and particles leads to an increase in Al-Li alloys hardness.

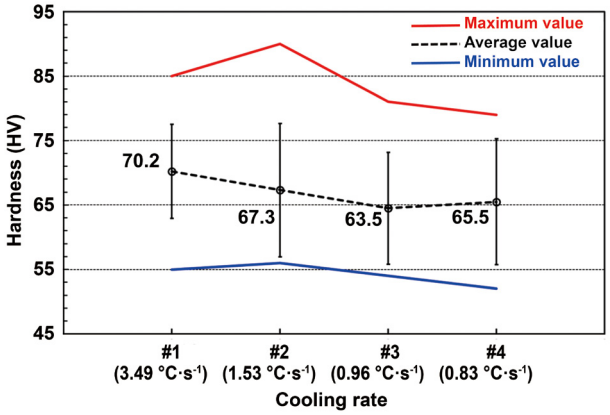

Fig. 9: Hardness of as-cast AA2297 Al-Li alloy as a function of cooling rates

Figure 10 shows the room temperature tensile properties of AA2297 Al-Li alloy at different cooling rates. The yield strength (YS), ultimate tensile strength (UTS) and elongation of Sample #4 with lower cooling rate are 112 MPa, 180 MPa and 4.7%, respectively, while the YS and UTS of Sample #1 with higher cooling rate at the surface of the ingot respectively reach 132 MPa and 219 MPa, and the elongation increases to 6.5%. YS, UTS, and elongation increase by 18%, 22% and 38%, respectively. The increase in cooling rate leads to grain refinement, and the reduction in the number of macropores may also contribute to the improvement of mechanical properties.

Figure 11 shows the room temperature tensile fracture morphology of the as-cast AA2297 Al-Li alloy at different cooling rates. At room temperature, the types of fractures are brittle, and the cooling rate has no significant effect on the fracture modes. However, as the cooling rate decreases, large pores appear on the fracture surface. It can be inferred that the fracture always occurs in the position with large pores during the tensile test, and the large pores will reduce the mechanical properties of the alloy.

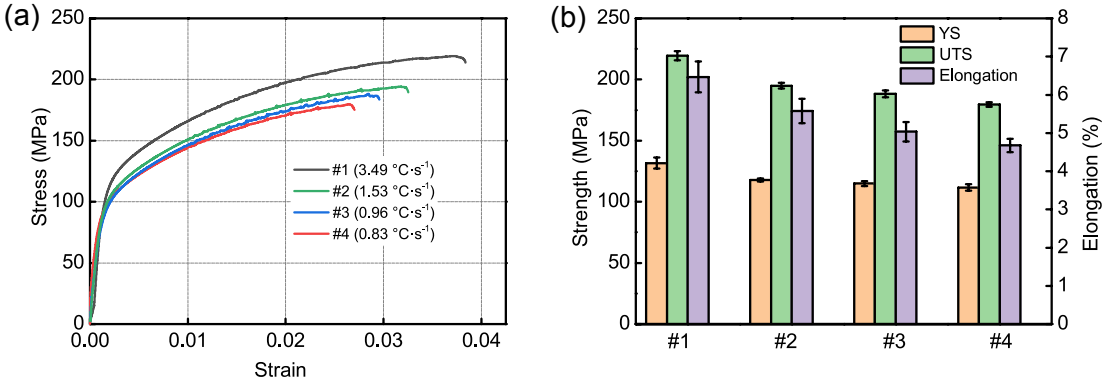

Fig. 10: Mechanical properties of as-cast AA2297 Al-Li alloy at different cooling rates: (a) engineering stress-strain curves; (b) comparison of YS, UTS, and elongation at four cooling rates

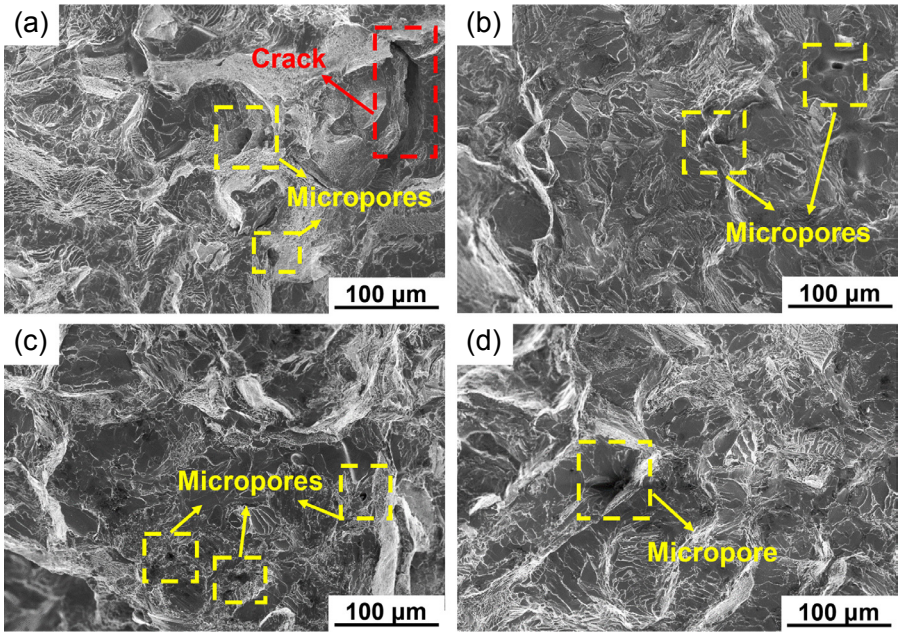

Fig. 11: Fracture surfaces of AA2297 Al-Li alloy stretched at room temperature under different cooling rates: (a) #1 at 3.49 °C·s^{-1}; (b) #2 at 1.53 °C·s^{-1}; (c) #3 at 0.96 °C·s^{-1}; (d) #4 at 0.83 °C·s^{-1}

3.4.2 Constitutive equation of AA2297 alloy

The true stress-strain curves below the solidus of the DC casting AA2297 Al-Li alloy were obtained through tensile tests at different temperatures and strain rates, as shown in Figs. 12(a), (c) and (e). After that, based on the extended Ludwik equation, the experimental values were fitted, and the stress sensitivity factors were obtained, as shown in Table 5. The predicted values are also plotted by curve fitting in Figs. 12(a), (c) and (e). The extended Ludwik equation has good predictability for the relationship between the stress and strain of the AA2297 Al-Li alloy below the solidus temperature.

Figures 12(b), (d) and (f) show the ultimate tensile strength and elongation of AA2297 Al-Li alloy at different strain rates and temperatures. It can be found that the mechanical properties of the alloys will be significantly different when tensile experiments are carried out at different temperatures. Taking the strain rate of 10^{-3} mm·s^{-1} as an example, the UTS decreases from 212 MPa to 50 MPa, and the elongation after

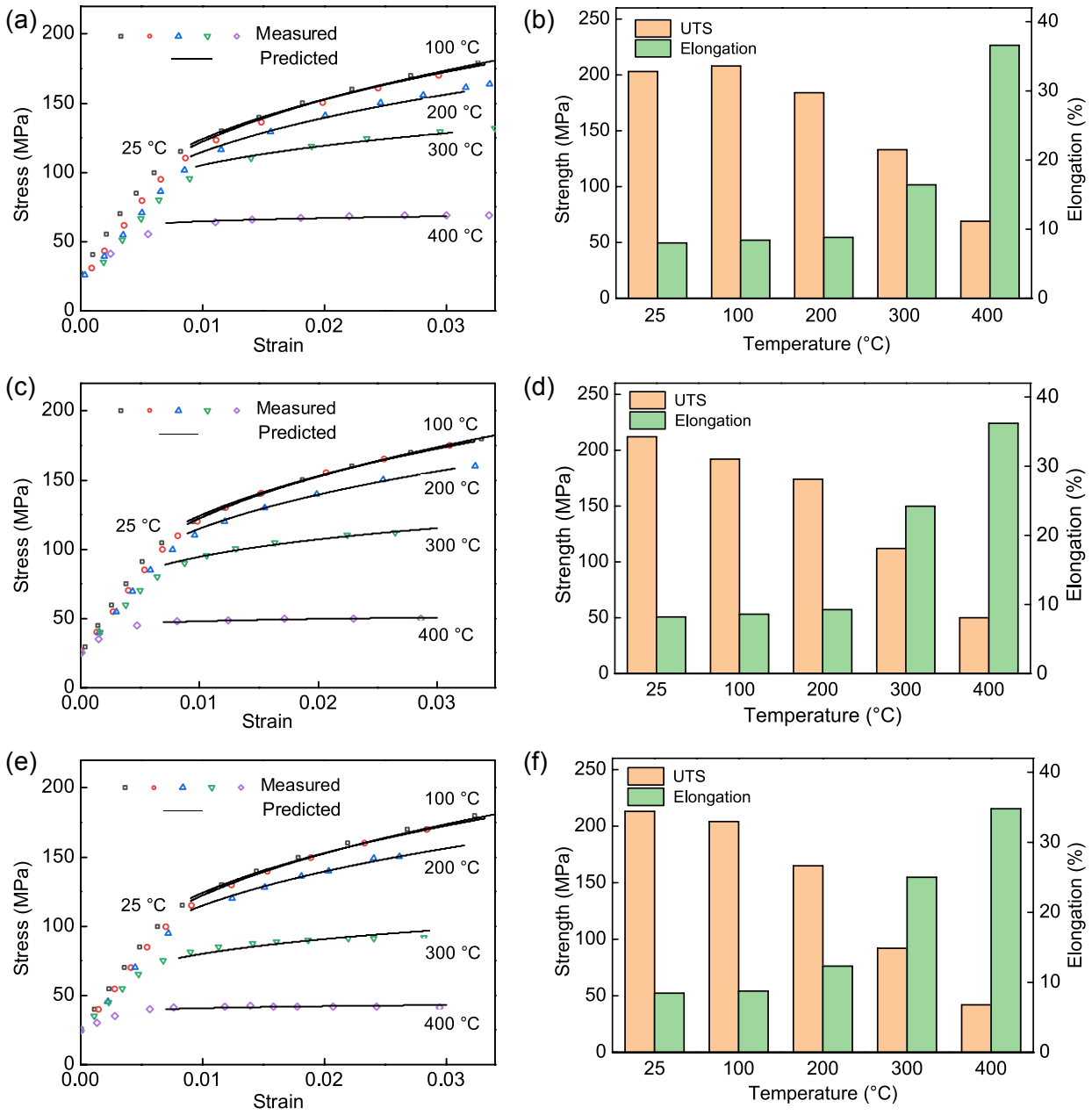

Fig. 12: Stress-strain curves (a, c, e) and tensile properties (b, d, f) of AA2297 Al-Li alloy at different temperatures and strain rates: (a, b) 10^{-2} mm·s^{-1}; (c, d) 10^{-3} mm·s^{-1}; (e, f) 10^{-4} mm·s^{-1}

Table 5: Parameter-temperature correlations for AA2297

Parameters	Temperature range (°C)	Values
K	$25 < T \le 160.3$	$K = -0.5232 \times T + 546.68$
	$160.3 < T \le 300$	$K = -1.1482 \times T + 646.87$
	$300 < T \le 400$	$K = -1.5141 \times T + 756.64$
n	$25 < T \le 227.3$	$n = -0.0002 \times T + 0.32$
	$227.3 < T \le 400$	$n = -0.0013 \times T + 0.57$
m	$25 \le T \le 200$	$m = 0$
	$200 < T \le 300$	$m = 0.000494T - 0.09879$
	$300 < T \le 400$	$m = 0.0008494T - 0.20541$

fracture increases from 8.20% to 36.20% with the increase of temperature. Below 200 °C, the change of strain rate has no significant effect on the properties of the alloy. But under high temperature conditions (above 200 °C), with the increase of strain rate, the elongation after fracture is increased and the UTS decreases obviously. The reason for this phenomenon may be due to the recrystallization of primary grains at temperature over 200 °C and dissolution of precipitates, leading to the increase of ductility and softening of matrix. In addition, the porosity may be arrested at the grain boundaries close to Fe-/Mn-rich particles or oxides, which leads to deterioration in the strength of the alloy.

4 Discussion

4.1 Effect of cooling rate on micropores

Sample #1 is located at the surface of the ingot and has the fastest cooling rate (3.49 °C·s^{-1}). Samples #2, #3, and #4 are successively away from the surface of the ingot and the cooling rates gradually decrease. In the position with fast cooling rate (#1), the internal pores are mainly small-sized micropores with high number density and large sphericity, while in the position with slow cooling rate, the internal pores are mainly irregular pores with low number density and small sphericity. The main reason for these phenomena is the large difference in cooling rate. On the one hand, the cooling rate has a significant effect on the number density of micropores. At fast cooling rates, the outer surface of the ingot solidifies first. Hydrogen separates very quickly from the solid phase, which causes an instantaneous increase in the hydrogen concentration in the liquid phase. The increase in the number of hydrogen nucleation leads to an increase in the amount density of micropores. While at slow cooling rates, the inside of the ingot is farther from the outer surface, and the micropores formed by the hydrogen separated from the solid phase have difficulty to escape from the outer solidified metal, but have enough time to aggregate and grow. Therefore, the number density of pores will decrease.

On the other hand, the cooling rate also has an effect on the volume and morphology of the micropores. The surface of the ingot has the fastest cooling rate, which belongs to the solidification chill part. The crystal grains are mainly fine dendrites, and the pores can only grow up after the dendrites are completely solidified. After the molten metal solidifies, the interdendritic area is narrow, and the restricted space limits the growth of micropores. In addition, the cooling rate is too fast, which shortens the time for the growth of pores, so the pores will show a small size and large sphericity. While at lower cooling rates, dendrites grow and their morphologies become irregular. The interdendritic region becomes larger, and the grain coarsening phenomenon is obvious. Compared with the outer surface, the center of the casting has a longer solidification time, and the micropore hydrogen absorption time is also longer. The micropores will aggregate and grow in the interstitial spaces of dendrites and intermetallic compounds, and finally form a large and complex morphology.

4.2 Influence of microstructure on mechanical properties

It can be seen from Figs. 9 and 10 that the Sample #1, with the fastest cooling rate during the casting process, has the best mechanical performance, while the Sample #4 has the worst performance. There are two reasons for this phenomenon. On the one hand, the difference in cooling rate results in significant differences in the grain size, and the compounds around the porosity contain harmful elements such as oxygen and iron after EDS energy spectrum analysis, which degrade the performance of the alloy. On the other hand, the microstructures such as micropores inside the alloy also have a significant impact on the mechanical properties of the alloy. At a high cooling rate (3.49 °C·s^{-1}), the pores in the alloy are mainly small hydrogen micropores that have not grown completely, so the alloy has a dense microstructure and high mechanical properties. At a slow cooling rate (0.83 °C·s^{-1}), the growth time of hydrogen micropores becomes longer, the interdendritic spaces are gradually filled with hydrogen, and the small hydrogen pores aggregate and grow into large-sized irregular pores. The higher internal porosity of the alloy reduces the loading area and tensile properties of the samples, and the large-sized irregular pores easily lead to cracks, resulting in premature fracture and failure of the aluminum alloy.

In order to further analyze the internal fracture causes of Al-Li alloy, Fig. 13 shows the SEM image of tensile fracture at different temperatures. It can be found that the shapes of pores and cracks at 25 °C, 100 °C and 200 °C are irregular, the volume is small, and secondary cracks appear in individual positions; the pores at high temperatures above 300 °C are mostly spherical and the volume is larger. Moreover, a large number of intermetallic compounds are also distributed around the pores on the tensile fracture. Point scanning and surface scanning were carried out respectively, and it is found that the main component is an intermetallic compound rich in iron/manganese, indicating that the iron/manganese-rich phase produced during the solidification process will adversely affect the mechanical properties of the alloy.

5 Conclusions

In this study, the influence of cooling rate on the number, morphology, and size of microporosity in the DC casting AA2297 Al-Li alloy was quantified, and statistical analysis on the correlation between microporosity and mechanical properties was performed. The following conclusions can be drawn:

(1) Increasing the cooling rate from 0.83 °C·s^{-1} to 3.49 °C·s^{-1} would result in the refinement of grain sizes, increase number density of micropores, and shorten the growth time of the micropores leading to the number density of pores in the 5–7 μm range growing from 150 to about 230 mm^{-3}, and reduction of the maximum equivalent diameter from 76.48 μm to 30.50 μm.

(2) The mechanical properties are largely influenced by the microstructure and microporosity. Large numbers of

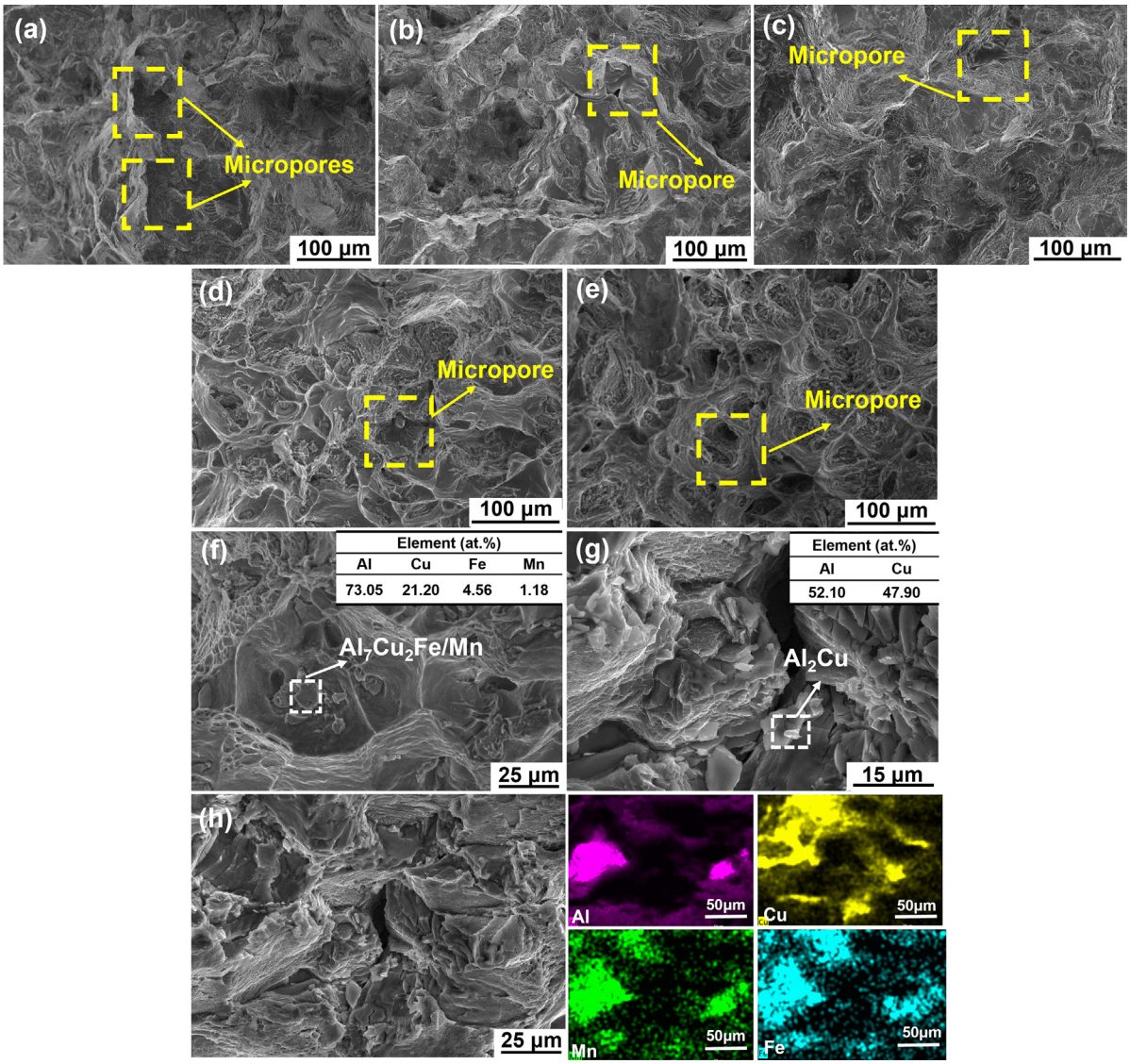

Fig. 13: Tensile fracture morphologies and EDS chemical analysis at different temperatures at a strain rate of 10^{-3} mm·s^{-1}: (a) 25 °C; (b) 100 °C; (c) 200 °C; (d) 300 °C; (e) 400 °C; (f) Al-Cu-Fe/Mn intermetallic compound point scanning analysis at 300 °C; (g) Al-Cu intermetallic compound point scanning analysis at 200 °C; (h) fracture surface scanning composition analysis at 200 °C

intermetallic compounds at the fracture surface of the alloy are also observed using SEM showing impurity elements such as oxygen, and iron. In addition, pores and cracks are irregular in shape and small at low temperature; most of the pores at high temperature above 300 °C are spherical and large in volume due to the Ostwald ripening.

(3) The constitutive equation of AA2297 Al-Li alloy was constructed based on the tensile test results at different temperatures and strain rates. Great agreement was achieved by this constitutive equation for the relationship between stress and strain in AA2297 Al-Li alloys.

Acknowledgements

The authors wish to express thanks for all the help from the lab mates at the Integrated Computational Materials Engineering (ICME) lab, Beijing Institute of Technology, China. Zeiss (Beijing) and the Experimental Center of Advanced Materials at Beijing Institute of Technology are greatly appreciated for their experiment support. The raw materials from Chinalco Southwest Aluminium (Group) Co., Ltd. are also greatly acknowledged. This research work was supported by the National Natural Science Foundation of China (Project number: 52073030).

References

[1] Phillion A B, Cockcroft S L, Lee P D. Predicting the constitutive behavior of semi-solids via a direct finite element simulation: Application to AA5182. Modelling and Simulation in Materials Science and Engineering, 2009, 17(5): 055011.

[2] Couper M J, Neeson A E, Griffiths J R. Casting defects and the fatigue behavior of an aluminium casting alloy. Fatigue Fract. Eng. Mater. Struct., 2010, 13: 213–227.

[3] Rioja R J, Liu J. The evolution of Al-Li base products for aerospace and space applications. Metallurgical & Materials Transactions A, 2012, 43(9): 3325–3337.

[4] Wanhill R, Bray G H. Fatigue crack growth behavior of aluminum-lithium alloys. Elsevier Inc: Netherlands, 2014: 381–413.
[5] Wang F Y, Wang X J, Cui J Z. Micro-structure and mechanical properties of 2A97 Al-Li alloy cast by low-frequency electromagnetic casting. Metals-Open Access Metallurgy Journal, 2019, 9(8): 822.
[6] Chen X X, Zhao G Q, Liu G L, et al. Microstructure evolution and mechanical properties of 2196 Al-Li alloy in hot extrusion process. Journal of Materials Processing Technology, 2019, 275: 116348.
[7] Vreeman C J, Schloz J D, Krane M J M. Direct chill casting of aluminum alloys: Modeling and experiments on industrial scale ingots. ASME, 2002, 124: 947–953.
[8] Luo Y J, Zhang Z F. Numerical modeling of annular electromagnetic stirring with intercooling in direct chill casting of 7005 aluminum alloy billet. Progress in Natural Science: Materials International, 2019, 29(1): 88–94.
[9] Skallerud B, Hrkegrd G, Iveland T, et al. Fatigue life assessment of aluminum alloys with casting defects. Engineering Fracture Mechanics, 1993, 44(6): 857–874.
[10] Akhtar N, Akhtar W, Wu S J. Melting and casting of lithium containing aluminium alloys. International Journal of Cast Metals Research, 2015, 28(1): 1–8.
[11] Gu J L, Yang S L, Gao M J, et al. Micropore evolution in additively manufactured aluminum alloys under heat treatment and inter-layer rolling. Materials & design, 2019, 186: 108288.
[12] Gu C, Lu Y, Luo A A. Three-dimensional visualization and quantification of microporosity in aluminum castings by X-ray micro-computed tomography. Journal of Materials Science and Technology, 2020, 65: 99–107.
[13] Wang J S. Physical metallurgy of aluminum alloys. In: Anderson K, Weritz J, and Kaufman G (Eds.), ASM Handbook, Aluminum and Aluminum Alloys, 2018, 2A: 44–79.
[14] Ding Z Y, Hu Q D, Lu W Q, et al. In-situ study on hydrogen bubble evolution in the liquid Al/solid Ni interconnection by synchrotron radiation X-ray radiography. Journal of Materials Science & Technology, 2019, 35(7): 1388–1392.
[15] Wang J S. Aluminum alloy ingot casting and continuous processes. Aluminum Science and Technology, ASM Handbook, 2018, 108–115.
[16] Lee P D, Hunt J D. Hydrogen porosity in directionally solidified aluminium-copper alloys: A mathematical model. Acta Materialia, 2001, 49(8): 1383–1398.
[17] Zhang Q Y, Wang T T, Yao Z J, et al. Modeling of hydrogen porosity formation during solidification of dendrites and irregular eutectics in Al-Si alloys. Materialia, 2018, 15(4): 211–220.
[18] Anyalebechi P N, Talbot D E J, Granger D A. The solubility of hydrogen in solid binary aluminum-lithium alloys. Metallurgical Transactions B, 1989, 20(4): 523–533.
[19] Anyalebechi P N. Analysis of the effects of alloying elements on hydrogen solubility in liquid aluminum alloys. Scripta Metallurgica et Materialia, 1995, 33(8): 1209–1216.
[20] Anyalebechi P N. Attempt to predict hydrogen solubility limits in liquid multicomponent aluminum alloys. Scripta Materialia, 1996, 34(4): 513–517.
[21] Smith S W, Scully J R. The identification of hydrogen trapping states in an Al-Li-Cu-Zr alloy using thermal desorption spectroscopy. Metallurgical & Materials Transactions A, 2000, 31(1): 179–193.
[22] Lee P D, Atwood R C, Dashwood R J, et al. Modeling of porosity formation in direct chill cast aluminum-magnesium alloys. Materials Science & Engineering A, 2002, 328(1–2): 213–222.
[23] Lee P D, Wang J S. Modeling of porosity formation during solidification. Metals Process Simulation, ASM Handbook, 2010, 22B: 253–263.
[24] Chaijaruwanich A, Dashwood J, Lee P D, et al. Pore evolution in a direct chill cast Al-6 wt.% Mg alloy during hot rolling. Acta Materialia, 2006, 4: 5185–5194.
[25] Chaijaruwanich A, Lee P D, Dashwood R J, et al. Evolution of pore morphology and distribution during the homogenization of direct chill cast Al-Mg alloys. Acta Materialia, 2007, 55(1): 285–293.
[26] Wang J S, Lee P D, Simulating tortuous 3D morphology of microporosity formed during solidification of Al-Si-Cu alloys. International Journal of Cast Metals Research. 2007, 20(3): 151–158.
[27] Wang J S, Lee P D, Hamilton R W, et al. The kinetics of Fe-rich intermetallic formation in aluminium alloys: In situ observation. Scripta Materialia, 2009, 60(7): 516–519.
[28] Wang J S, Li M, Allison J, et al. Multiscale modeling of the influence of Fe content in a Al-Si-Cu alloy on the size distribution of intermetallic phases and micropores. Journal of Applied Physics, 2010, 107(6): 061804.
[29] Phillion A B, Cockcroft S L, Lee P D. A new methodology for measurement of semi-solid constitutive behavior and its application to examination of as-cast porosity and hot tearing in aluminum alloys. Materials Science and Engineering: A, 2008, 491(1–2): 237–247.
[30] Dou R F, Phillion A B. Application of a pore fraction hot tearing model to directionally solidified and direct chill cast aluminum alloys. Metallurgical and Materials Transactions A: Physical Metallurgy and Materials Science, 2016, 47: 4217–4225.
[31] Chen D X, Dou R F, Han J Q, et al. Prediction of hot tearing susceptibility of direct chill casting of AA6111 alloys via finite element simulations. Transactions of Nonferrous Metals Society of China, 2020, 30(12): 3161–3172.
[32] Hao H, Maijer D M, Wells M A, et al. Development and validation of a thermal model of the direct chill casting of AZ31 magnesium billets. Metallurgical & Materials Transactions A, 2004, 35(12): 3843–3854.
[33] Baserinia A R, Ng H, Weckman D C, et al. A Simple model of the mold boundary condition in direct-chill (DC) casting of aluminum alloys. Metallurgical & Materials Transactions B, 2012, 43(4): 887–901.
[34] Gu J L, Gao M J, Yang S L, et al. Pore formation and evolution in wire + arc additively manufactured 2319 Al alloy. Additive Manufacturing, 2019, 30: 100900.
[35] Xue C P, Zhang Y X, Mao P C, et al. Improving mechanical properties of wire arc additively manufactured AA2196 Al-Li alloy by controlling solidification defects. Additive Manufacturing, 2021, 43: 102019.
[36] Alankar A, Wells M A. Constitutive behavior of as-cast aluminum alloys AA3104, AA5182 and AA6111 at below solidus temperatures. Materials Science and Engineering: A, 2010, 527(29–30): 7812–7820.
[37] Chen R, Wang H M, He B, et al. Effect of thermal cycling on microstructure and mechanical properties of 2A97 Al-Li alloy fabricated by direct laser deposition. Vacuum, 2021, 190: 110299.
[38] Zhou Y H, Lin X, Kang N, et al. Influence of travel speed on microstructure and mechanical properties of wire + arc additively manufactured 2219 aluminum alloy. Journal of Materials Science & Technology, 2020, 37: 143–153.
[39] Kastner J, Harrer B, Peter Degischer H. High resolution cone beam X-ray computed tomography of 3D-microstructures of cast Al-alloys. Materials Characterization, 2011, 62(1): 99–107.
[40] Wang B, Zhang M S, Wang J S. Quantifying the effects of cooling rates and alloying additions on the microporosity formation in Al alloys. Materials Today Communications, 2021, 28: 102524.